Mathematics and Computers in Simulation 233 (2025) 369–388

Contents lists available at ScienceDirect

Mathematics and Computers in Simulation

journal homepage: www.elsevier.com/locate/matcom

Original articles

Vertical modeling of carbon sequestration in coastal wetlands using fractional-order derivatives and moisture dynamics

Vsevolod Bohaienko [a], Fasma Diele [a,*], Fabio V. Difonzo [a,d], Carmela Marangi [a], Angela Martiradonna [b,a], Antonello Provenzale [c]

[a] Istituto per le Applicazioni del Calcolo M.Picone, Consiglio Nazionale delle Ricerche, via Amendola 122/D, Bari, 70126, Italy
[b] Department of Economics, University of Foggia, Via Caggese 1, Foggia, 71121, Italy
[c] Institute of Geosciences and Earth Resources, Consiglio Nazionale delle Ricerche, via G. Moruzzi 1, Pisa, 56124, Italy
[d] Departement of Engineering, LUM University Giuseppe Degennaro, S.S. 100 km 18, Casamassima (BA), 70010, Italy

ARTICLE INFO

MSC:
26A33
86-08
68U20
65M06

Keywords:
Wetlands
Carbon dynamics
RothC model
Richardson–Richard's equation
Fractional-order derivatives
Greenhouse gas emissions

ABSTRACT

Wetlands are essential for global biogeochemical cycles and ecosystem services, with the dynamics of soil organic carbon (SOC) serving as the critical regulatory mechanism for these processes. However, accurately modeling carbon dynamics in wetlands presents challenges due to their complexity. Traditional approaches often fail to capture spatial variations, long-range transport, and periodical flooding dynamics, leading to uncertainties in carbon flux predictions. To tackle these challenges, we introduce a novel extension of the fractional RothC model, integrating temporal fractional-order derivatives into spatial dimensions. This enhancement allows for the creation of a more adaptive tool for analyzing SOC dynamics. Our differential model incorporates Richardson–Richard's equation for moisture fluxes, a diffusion–advection–reaction equation for fractional-order dynamics of SOC compounds, and a temperature transport equation. We examine the influence of diffusive movement and sediment moisture content on model solutions, as well as the impact of including advection terms. Finally, we validated the model on a restored wetland scenario at the Ebro Delta site, aiming to evaluate the effectiveness of flooding strategies in enhancing carbon sequestration and ecosystem resilience.

1. Introduction

Wetlands, characterized by their dynamic hydrological regimes and diverse vegetation, have significant influence on global biogeochemical cycles and ecosystem service provision. Central to the functioning of wetlands are the interconnections among biotic and abiotic factors, with soil carbon dynamics serving as a cornerstone in regulating ecosystem processes and preserving their ecological services. In contrast to upland forests and rangelands, wetlands undergo extended periods of sediment oxygen depletion, leading to specialized adaptations in vegetation for anaerobic conditions. Despite these conditions, wetlands also experience periods of sediment aeration and unsaturation, resulting in a diverse range of valuable ecosystem services [1].

Wetlands are vital hubs for a range of ecosystem services falling within the four categories delineated by the Millennium Ecosystem Assessment [2], covering provisioning, regulating, cultural, and supporting services. The majority of these services are closely tied to the water cycle and wield significant economic influence on both local and global scales. The economic significance of wetlands extends beyond the tangible products they offer, e.g. fresh water, food, timber, and pharmaceuticals [3]. Their regulatory services, not only contribute to mitigate natural hazards, but also actively bolster circular economy strategies, e.g by exploiting water

* Corresponding author.
E-mail address: fasma.diele@cnr.it (F. Diele).

https://doi.org/10.1016/j.matcom.2025.02.005
Received 29 June 2024; Received in revised form 28 January 2025; Accepted 3 February 2025
Available online 15 February 2025

purification. Additionally, well preserved wetlands supports other ecosystems with even higher monetary value. All in all, a recent estimate suggests that the services rendered by wetlands are monetarily valued at approximately Int$47 trillion annually [4]. Due to the aforementioned factors, allocating funds towards coastal management and restoration can yield substantial economic benefits in the long run, surpassing the initial expenses incurred for preservation. The imperative for restoration grows as the degradation and loss of coastal wetlands outpace that of other ecosystems, significantly diminishing the provision of ecosystem services. One of the adverse consequences of degradation is its influence on the carbon cycle, potentially reducing the carbon storage ability of wetlands or even transforming them from natural carbon sinks into sources.

Understanding the sediment carbon cycle in wetlands is essential for addressing broader environmental issues, particularly in the context of climate change mitigation and adaptation. Wetlands are among the most effective natural carbon sinks, sequestering atmospheric carbon dioxide through the accumulation of organic matter in anaerobic sediment conditions. Nonetheless, in some cases, the release of potent greenhouse gases like methane can counteract their climate mitigation potential. The complexity of wetland ecosystems poses challenges for accurately modeling carbon dynamics, hindering our ability to predict ecosystem responses to environmental changes and inform effective management strategies [5]. It is thus essential to clarify the distinction between various types of wetlands, including floodplains, peatlands, etc, each of which has unique characteristics and is often modeled with dedicated approaches tailored to its specific dynamics. The hydrodynamic regime characteristic of coastal wetlands differs significantly from that of peatlands, motivating the need for a specialized model tailored to the unique conditions present in coastal regions. Our study specifically focuses on coastal wetlands where tidal influence plays a significant role, creating environmental and hydrological conditions that are markedly different from those found in internal freshwater wetlands or peatlands, where tidal impacts are not present. Thus, peatland models, while also addressing carbon storage functions, are not directly transferable to our study's context. In particular, the peatland models in [6,7] describe specific processes such as the influence of peat formation on poroelastic properties of soil. These processes are peculiar for peatlands but not for wetlands in general.

Simplistic modeling approaches often fall short in capturing the hydro-physical properties and non-linear dynamics inherent in wetland sediments [8]. Many wetland nutrient cycling models employ a simplified internal mass balance equation to simulate groundwater levels based solely on precipitation and evapotranspiration losses [9]. This approach often results in a representation where wetlands are primarily influenced from above, neglecting the significant impact of groundwater vertical movements, characteristic of wetland environments. Another aspect that requires special consideration is the seasonal pattern of water level in wetlands and the rise and fall of wetland surface and subsurface water. Traditional models able to describe variably-saturated wetland conditions by tracking moisture in wetland sediment [10] overlook processes such as long-range transport, spatial variations in sediment properties and periodical flooding, leading to uncertainties in carbon and methane flux predictions and, consequently, in ecosystem assessments. Finally, no existing model adequately captures the memory effects on SOC dynamics, which may arise from processes that are not explicitly modeled, such as mass exchange between substances in dissolved and solid states.

To address these limitations, there is a growing need for modeling techniques that can capture the complexities of wetland ecosystems and provide robust predictions of carbon cycling dynamics. Integrated models such as those developed in [11] focus on carbon dynamics and methane emissions driven by hydrology, sediment biogeochemistry, and vegetation processes. Models like Estimation of Carbon in Organic Soils—Sequestration and Emissions (ECOSSE) [12] predict the impact of land-use and climate change on greenhouse gas emissions, incorporating sediment carbon and nitrogen turnover processes. The Peatland Carbon Simulator (PCARS) [13] simulates the carbon balance in peatlands, incorporating components such as plant photosynthesis, decomposition, methane production, and loss of dissolved organic carbon with drainage water. As wetlands exhibit distinct redox gradients, with anaerobic conditions prevailing in deeper layers and influencing microbial processes and methane production, vertical layer models for SOC dynamics are crucial for understanding the complex interplay of hydrological and ecological factors across different sediment depths.

In this paper, we introduce a novel extension of the original RothC model (12) incorporating temporal fractional-order derivatives into a spatially-extended domain, to enhance the accuracy of wetland modeling. By extending the fractional version of this model introduced in [14] to incorporate spatial dimensions, we aim to generalize some spatially explicit RothC approaches found in the literature [12,15–17] and offer a more comprehensive understanding of sediment carbon dynamics in the specific case of coastal wetlands [18]. In particular, we investigate the impact of vertical layers in modeling carbon decomposition dynamics within the substrate, emphasizing the interplay between hydrological and biological factors across varying sediment depths, with a particular focus on microbial processes and methane production over carbon dioxide.

We develop a differential model that relies on several key components. First, we utilize the Richardson–Richards equation (RRE) to simulate moisture fluxes [19,20]. Then, we integrate a diffusion–advection–reaction equation for simulating the fractional order dynamics of SOC compounds within a vertical layer. This is coupled with a decomposition rate modifier delineating the transition from aerobic bacterial activity generating CO_2 to anaerobic bacterial activity producing CH_4 in water-saturated sediments. Lastly, we incorporate a temperature transport equation influencing the dynamics at varying depths. Additionally, we introduce specific boundary conditions to simulate periodic flooding. Our model allows to examine how diffusive movement and transport due to sediment moisture fluxes influence the solutions of sediment organic carbon compound equations in the substrate. By comparing solutions with and without advection, we aim to elucidate the role of the new features introduced here in order to understand how advection influences SOC dynamics in wetland ecosystems. Furthermore, we assess the plausibility of modeling wetland restoration scenarios using our novel model. By simulating flooding scenarios and comparing model outcomes with empirical data, we aim to evaluate the effectiveness of restoration strategies in enhancing carbon sequestration.

The paper is organized as follows. In Section 2, we introduce the RRE formulation for saturated–unsaturated sediments and establish specific boundary conditions to model water level fluctuations in coastal wetlands, complemented by meteorological

inputs. Section 3 extends the fractional RothC model vertically across the sediment column, integrating constant diffusion and advection driven by water infiltration velocity, the latter derived from RRE. Moving to Section 4, we develop formulations for carbon dioxide (CO_2) and methane (CH_4) emissions, which are related to aerobic or anaerobic bacterial respiration. In Section 5, we provide simulations, exploring the impacts of periodic flooding and sediment moisture fluxes on carbon stocks and greenhouse gas emissions, particularly in the Ebro Delta wetland restoration context. Finally, we wrap up with a discussion, concluding remarks, and future research avenues. Appendices include details on the numerical scheme and computational issues (Appendix A) and the numerical evaluation of greenhouse gas fluxes (Appendix B).

2. Soil moisture fluxes and periodical flooding in wetlands

The modeling of water infiltration in sediment is based on the Richardson–Richards equation [19,21,22], which is an advection–diffusion equation derived by conservation of mass that extends Darcy's law for saturated flow in porous media. Our emphasis is on the vertical dimension in infiltration, predominantly influenced by gravity.

We introduce the water head pressure function $h(z,t)$, representing the potential energy of water in the sediment measured as the height of the water column above the depth level z at time t. When $h(z,t)=0$, the level z aligns with the water table position at time t, marking the boundary between saturated and unsaturated sediment zones. Positive values of h indicate points below the water table, corresponding to the saturated zone where all sediment pores are filled with water. Conversely, negative values of h indicate points above the water table, corresponding to the unsaturated zone where both air and water coexist in the sediment pores.

There are two reasons that motivated the use of an unsaturated/saturated flow equation: one is that we wanted to address the carbon sequestration in wetlands whose state is changed from agricultural usage to a reclaimed state. In this case, and also under the influence of climate changes, soil layers next to the surface can become non-saturated (or are forced to become non-saturated for the needs of farming) even in wetlands. Analogously, in the case of a paddy rice field—a form of agricultural practice in which surface flooding is applied along with the natural flooding processes—the approach followed here allows us to capture the variable saturation conditions. These dynamics are essential for representing the water movement and soil moisture interactions within these systems, where fully saturated models would not effectively capture the fluctuations between different saturation states. For saturated/unsaturated sediments, the one-dimensional Richards equation, known as Richardson–Richards equation (RRE), when expressed in relation to the water head pressure $h(z,t)$ [L], has the following expression, as outlined in [23]:

$$\left(C(h)+S_e(h)\,S_s\right)\frac{\partial h}{\partial t}=\frac{\partial}{\partial z}\left(K(h)\left(\frac{\partial h}{\partial z}-1\right)\right). \tag{1}$$

In this equation, t [T] is the time, z [L] is the spatial coordinate (positive downwards), and $K(h)$ [L T^{-1}] denotes the hydraulic conductivity function. The dimensionless function $S_e(h)$ represents the effective saturation and S_s [L^{-1}] is the specific storage value. The function $C(h)$ [L^{-1}] represents the specific moisture capacity and is defined as the spatial derivative of the water retention curve $\theta(h)$ [–]. The term $v(z,t)$ [L T^{-1}] is defined as

$$v(z,t)=K(h)\left(\frac{\partial h}{\partial z}-1\right) \tag{2}$$

and it measures the vertical water flux according to the Darcy's law.

The function $S_e(h)$ exhibits two distinct types of behavior based on the pressure head, depending on whether the porous media is saturated or not, as in [24]:

$$S_e(h)=\begin{cases}\left(1+(-a\,h)^n\right)^{-m}, & if\ h<0\\ 1, & if\ h\geq 0\end{cases}$$

where $m=1-\frac{1}{n}$. The functional dependencies of $\theta(h)$ and $K(h)$ on h are handled using the van Genuchten–Mualem functions and the related empirical parameters $a>0$ [L^{-1}] and $n>0$, for unsaturated conditions [25,26]. The expression of the water retention curve (or volumetric moisture content) is given by

$$\theta(h)=\theta_r+(\theta_s-\theta_r)\,S_e(h) \tag{3}$$

where θ_r is the residual moisture content, θ_s is the saturated moisture content. Consequently,

$$C(h)=\frac{d\theta}{dh}=\frac{a\,m}{1-m}(\theta_s-\theta_r)\,S_e^{1/m}(h)\left(1-S_e^{1/m}(h)\right)^m.$$

Finally, the hydraulic conductivity is defined as

$$K(h)=K_s\,S_e^{\eta}(h)\left(1-\left(1-S_e^{1/m}(h)\right)^m\right)^2 \tag{4}$$

where K_s [L T^{-1}] is the filtration coefficient (hydraulic conductivity at the saturated state) and η is another empirical parameter. In the saturated sediment zone, when $h\geq 0$, it holds that $S_e(h)=1$ and $\theta(h)=\theta_s$. As a consequence, $C(h)$ drops to zero and $K(h)$ maintains the constant value K_s. This leads to the following simplification of Eq. (1) under saturated conditions:

$$S_s\frac{\partial h}{\partial t}=\frac{\partial}{\partial z}\left(K_s\left(\frac{\partial h}{\partial z}-1\right)\right). \tag{5}$$

2.1. Boundary conditions

On the upper boundary, at $z = 0$, Eq. (1) is subject to the following condition:

$$q(t) = -K(h(0,t))\left(\frac{\partial h}{\partial z}(0,t) - 1\right) = P(t) - E(t). \tag{6}$$

Here, $E(t)$ [$\mathrm{L\,T^{-1}}$] represents evapotranspiration, which is considered to influence only the upper boundary layer of the sediment when it is not submerged, neglecting the portion of moisture removed from the sediment by plants and their root systems, while $P(t)$ [$\mathrm{L\,T^{-1}}$] denotes precipitation.

We consider time-variant boundary conditions at the lower boundary $z = l$ of the simulation domain by setting the water head pressure $h(l,t)$ to be equal to $l - l_e(t)$, where $l_e(t)$ is the water level in an external source (sea, river, or lake) of groundwater in the sediment column [27]:

$$h(l,t) = l - l_e(t). \tag{7}$$

Further, for the condition (6) we set $q(t) = 0$ when $l_e(t) \le 0$. Such condition follows from the assumption that for coastal wetlands, which are the main subject of this study, the influence of evapotranspiration and precipitation on the level of water above the sediment surface can be considered negligible.

Using this approach, and following [24], we assume a unidirectional influence of external surface water sources on groundwater levels. In our model, the value of $l_e(t)$ is an external input and should be determined through measurements or additional modeling of flooding processes. By setting the external water source level as $l_e(t)$, we assume that the transitional processes of surface water influence on the water table occur within a negligible time frame.

Well-posedness of Eq. (1) with boundary conditions (6) and (7) is a broadly studied topic about parabolic partial differential equations; however, the mixed Dirichlet-Neumann boundary conditions and the regularity of $C(h) + S_e(h)S_s$, multiplying the partial temporal derivative on the left-hand side of (1), make the problem delicate, both for extending it to higher dimensions, and because the problem itself changes nature when the saturated zone is reached.

To infer existence and uniqueness of (1) with the boundary conditions (6) and (7), one could resort to regularization techniques [28], or frame the problem using functional analysis tools [29]. In both cases, obtaining stronger regularity for the solution could be an issue, and further results with different techniques could be found in [30]; moreover, we refer to [31] for considerations on mixed boundary conditions and regularity thereof.

2.2. Steady-state solution

By denoting with $\bar{q}$ a constant vertical water flux and $\bar{l}_e$ a constant elevation of the water level in the external source, the downward water flux $\bar{h}(z)$ solves the steady-state state RRE:

$$\frac{d}{dz}\left(K(\bar{h})\left(\frac{d\bar{h}}{dz} - 1\right)\right) = 0, \quad z \in [0, l] \tag{8}$$

subject to the boundary conditions

$$-K(\bar{h}(0))\left(\frac{d\bar{h}}{dz}(0) - 1\right) = \bar{q}, \quad \bar{h}(l) = l - \bar{l}_e. \tag{9}$$

Then, the flux along the column remains constant at the value of $\bar{q}$:

$$-K(\bar{h}(z))\left(\frac{d\bar{h}}{dz}(z) - 1\right) = \bar{q}, \quad z \in [0, l]. \tag{10}$$

and the steady-state solution satisfies the following final value problem:

$$\begin{aligned} \frac{d\bar{h}}{dz} &= 1 - \frac{\bar{q}}{K(\bar{h})}, \quad z \in [0, l] \\ \bar{h}(l) &= l - \bar{l}_e. \end{aligned} \tag{11}$$

We will utilize the steady-state solution in our simulations to estimate the initial distribution of the water head $h_0(z)$ for RRE (1).

3. In-depth fractional RothC model

The RothC model, originally developed to simulate soil organic carbon dynamics within agricultural systems [32,33], offers a robust framework for understanding carbon cycling processes across various contexts [34–36] and scales [37]. Moreover, it has been effectively integrated into broader land surface models [16]. This model categorizes soil organic carbon (SOC) dynamics into four active compartments, representing distinct stages of organic matter decomposition and cycling: decomposable plant material (DPM),

resistant plant material (RPM), microbial biomass (BIO), humus (HUM). Following the notation in [34], the classical RothC model can be represented as:

$$\frac{d\mathbf{c}}{dt} = \rho(t)\, A\, \mathbf{c} + \mathbf{b}(t), \quad A = \begin{bmatrix} -k_{\mathrm{dpm}} & 0 & 0 & 0 \\ 0 & -k_{\mathrm{dpm}} & 0 & 0 \\ \alpha k_{\mathrm{dpm}} & \alpha k_{\mathrm{rpm}} & (\alpha-1)k_{\mathrm{bio}} & \alpha k_{\mathrm{hum}} \\ \beta k_{\mathrm{dpm}} & \beta k_{\mathrm{rpm}} & \beta k_{\mathrm{bio}} & (\beta-1)k_{\mathrm{hum}} \end{bmatrix} \tag{12}$$

where $\mathbf{c}(t) = [c_{\mathrm{dpm}}(t), c_{\mathrm{rpm}}(t), c_{\mathrm{bio}}(t), c_{\mathrm{hum}}(t)]^{\top}$ is a vector containing the concentrations of the different carbon pools at time t, and $\mathbf{b}(t) = [\gamma, 1-\gamma, 0, 0]^{\top} g(t)$ is a vector representing the allocation of litter input $g(t)$ between DPM and RPM pools. This partition is based on the coefficient γ satisfying the relation $\frac{\gamma}{1-\gamma} = r$, where the DPM/RPM ratio r provides an estimate of the decomposability of the incoming plant material. The matrix A describes the interactions and transformations between the carbon pools, governed by the decomposition rate constants k_{dpm}, k_{rpm}, k_{bio}, and k_{hum}. Parameters α and β represent the proportion of carbon incorporated into the BIO and HUM compartments, which is determined by the percent of clay content of the sediment (clay), according to [32]

$$\alpha = \frac{0.46}{x+1}, \quad \beta = \frac{0.54}{x+1}, \qquad x = 1.67\,(1.85 + 1.60\, e^{-0.0796\,\mathrm{clay}}).$$

The residual fraction $1-(\alpha+\beta)$ is released into the atmosphere as CO_2. Finally, the rate modifier $\rho(t)$ depends on temperature, moisture and soil cover [32].

The vertical representation of the RothC model, introduced in [15], accounts for the distribution of carbon across multiple vertical layers. It includes vertical mixing (diffusion) and transport due to water movement, allowing for a more detailed and accurate representation of decomposition processes and carbon transfer within the soil. The model with vertical mixing, excluding the transport term, was further analyzed in [16] and integrated into the Joint UK Land-Environment Simulator (JULES), with a specific focus on permafrost regions.

In the following, we first introduce the vertical representation of the RothC model, incorporating an advection term, under the assumption that the transport of SOC along the sediment column follows the same movement as water infiltration. Secondly, we generalize the model employing fractional calculus to offer enhanced modeling capabilities for SOC in wetland ecosystems.

3.1. In-depth integer-order RothC model

Vertical layers in wetlands play a crucial role in organic carbon dynamics in the sediment substrate due to unique ecological and hydrological conditions. Distinct redox gradients create anaerobic conditions in deeper layers, influencing microbial activity and decomposition processes. The water-saturated environment, along with varying root activities, leads to differential SOC accumulation and decomposition rates across vertical layers. Temperature gradients, water table fluctuations, and nutrient dynamics at different sediment depths contribute to the complex factors influencing SOC dynamics in wetlands. Recognizing the vertical dimension is essential for accurate assessments of carbon stocks, greenhouse gas emissions, and effective wetland conservation and management, especially in the context of climate change and evolving land-use patterns.

Assuming that the SOC concentrations vector $\mathbf{c}(z,t)$, [M L^{-3}], is a function of both time and depth, the model for the SOC dynamics is represented by the following partial differential system:

$$\frac{\partial \mathbf{c}}{\partial t} = \frac{\partial}{\partial z}\left(D\,\frac{\partial \mathbf{c}}{\partial z} - v(z,t)\,\mathbf{c}\right) + \rho(z,t)\, A\, \mathbf{c} + \mathbf{b}_d(z,t), \;\; z \in [0,l], \;\; t \geq t_0. \tag{13}$$

The diffusivity term in (13) is influenced by the diagonal matrix D, where each diagonal element D_i [L^{2}T^{-1}] represents the diffusivity coefficient in the ith compartment. If we confine the analysis to sufficiently small depths ($l \leq 1$), we can assume that the diffusion coefficients remain constant regardless of depth, as suggested in [38].

The transport term in (13) captures the dynamics of SOC within the column due to the sediment moisture fluxes $v(z,t)$ defined in (2), considering convective migration.

The source term $\mathbf{b}_d(z,t)$ [M L^{-3} T^{-1}] is related to the organic matter that is incorporated in the system in the form of root-derivative products [39] and we assume that it is modeled to decline exponentially with depth i.e.

$$\mathbf{b}_d(z,t) = \mathbf{B}_d(t)\, \frac{b_e\, e^{-b_e z}}{1 - e^{-b_e l}} \tag{14}$$

where $\mathbf{B}_d(t)$ [M L^{-2} T^{-1}] is the total input in the form of root-derivative products and $b_e > 0$ is an empirical parameter.

System (13) is initialized with the initial distribution $\mathbf{c}(z,0) = \mathbf{c}_0(z)$ and boundary conditions. We set a zero Neumann condition at the bottom and a controlled flux condition at the upper boundary of the domain to model the incoming flux $\mathbf{b}_s(t)$ [M L^{-2} T^{-1}], representing the carbon input from the decomposition of leaves or grass on the surface:

$$-\left[D\frac{\partial \mathbf{c}}{\partial z}(0,t) - v(0,t)\,\mathbf{c}(0,t)\right] = \mathbf{b}_s(t), \quad \frac{\partial \mathbf{c}}{\partial z}(l,t) = 0 \tag{15}$$

The zero Neumann condition imposed on the bottom of the soil column simulates free flow of dissolved substances through the boundary, assuming that the diffusion flow can be neglected compared to the advection flow. This condition transforms into a no-flow condition in the absence of water movement. Such assumption is reasonable when the impermeable bed is deep enough and the water table changes rapidly, thus allowing modeling only the part of the soil column where SOC dynamics is essential for further applications. The depth of the simulated column should thus ensure that the condition has negligible influence on SOC

dynamics.

In the RothC model [32], the rate modifier $\rho = \rho(z,t)$ is defined as the product of three factors $k_1(T_{\text{emp}})$, $k_2(s_\theta)$ and $k_3(c)$,[1]

$$\rho(z,t) = k_1(T_{\text{emp}})\, k_2(s_\theta)\, k_3(c),$$

depending on sediment temperature T_{emp}, saturation sediment moisture s_θ and sediment cover c, respectively. Let us analyze each of these factors.

Modeling the temperature factor $k_1(T_{\text{emp}})$. The factor $k_1(T_{\text{emp}})$ depends on the sediment temperature $T_{\text{emp}} = T_{\text{emp}}(z,t)$ obtained by solving the heat equation

$$C_{T_{\text{emp}}} \frac{\partial T_{\text{emp}}}{\partial t} = \frac{\partial}{\partial z}\left(\lambda \frac{\partial T_{\text{emp}}}{\partial z} - C_{T_{\text{emp}}} v(z,t) T_{\text{emp}}\right), \tag{16}$$

equipped by the initial condition $T_{\text{emp}}(z,0) = T_0(z)$ and the boundary conditions

$$T_{\text{emp}}(0,t) = T_a(t), \quad \frac{\partial T_{\text{emp}}}{\partial z}(l,t) = 0, \tag{17}$$

with $T_0(0) = T_a(0)$. Here $C_{T_{\text{emp}}}$ [M L^{-1} T^{-2} Q^{-1}] is the heat capacity, λ [ML T^{-3} Q^{-1}] is the thermal conductivity of the sediment, and $T_a(t)$ is the air temperature at time t. Note that the temperature field equation is connected to RRE through the velocity $v(z,t)$ appearing in the advection term.

Differently from [35], here we apply the following commonly used exponential function to model the k_1 factor:

$$k_1(T_{\text{emp}}(z,t)) = Q_{10}^{0.1 \frac{\overline{T}_{\text{emp}}(z)}{T_{\text{emp}}(z,t)}\left(T_{\text{emp}}(z,t) - \overline{T}_{\text{emp}}(z).\right)}$$

In the above formula, $T_{\text{emp}}(z,t)$ represents the sediment temperature, while $\overline{T}_{\text{emp}}(z)$ denotes a reference distribution, typically reflecting the mean temperature distribution within the analyzed area, both measured in Kelvin. The dimensionless value Q_{10} is fixed at 2, as in [16]. The expression of $k_1(T_{\text{emp}})$ ensures that when the temperature remains constant at its reference value (i.e. $T_{\text{emp}}(z,t) = \overline{T}_{\text{emp}}(z)$), the factor k_1 remains equal to 1. This implies that the degradation and respiration processes of SOC do not undergo variations due to temperature fluctuations, as the k_1 term does not affect their rates. Essentially, the model takes into account the temperature effect only when it deviates from the reference distribution.

Modeling the moisture factor $k_2(s_\theta)$. The decomposition rate factor $k_2(s_\theta)$ is linked to the saturation moisture factor $s_\theta = \theta/\theta_s$ where $\theta = \theta(h(z,t))$ is the moisture content given in (3) and θ_s is its saturated value. Assuming the permanent wilting point to be equal to the residual water content parameter θ_r in the van Genuchten model described in (3), when the sediment is dry (i.e., $\theta = \theta_r$), we assign the value of 0.2 to k_2. As moisture increases, k_2 linearly increases until it reaches its maximum value of 1 at the moisture content $\theta = \theta_0$, where $\theta_0 = 0.5\,(1 + \theta_r/\theta_s)\,\theta_s$. Afterward, k_b decreases until saturation is achieved ($\theta = \theta_s$). Introducing the constants $s_r = \theta_r/\theta_s$ and $s_0 = \theta_0/\theta_s$, the decomposition rate factor $k_2(s_\theta)$ is then defined as

$$k_2(s_\theta) = \begin{cases} 0.2, & \text{if } s_\theta = s_r \\ 1 - 0.8\,\dfrac{s_0 - s_\theta}{s_0 - s_r}, & \text{if } s_r < s_\theta \le s_0 \\ 1 - (1 - f_{anox})\,\dfrac{s_\theta - s_0}{1 - s_0}, & \text{if } s_0 < s_\theta \le 1, \end{cases}$$

and it achieves, at saturation, the value f_{anox}, representing a constant rate related to activity of CH_4-generating bacteria.

Modeling the sediment cover factor k_3. The coefficient $k_3 = k_3(c)$ is linked to the vegetation soil cover $c(t)$. In this context, we adopt the definition provided in [16], which defines the expression $k_3(c) = 0.6 - 0.4\,(c(t) - 1)$, where $0 \le c(t) \le 1$ represents the fraction of soil covered by vegetation, with $c(t) = 0$ denoting bare sediment and $c(t) = 1$ indicating fully vegetated sediment.

3.2. Fractional formulation of the model

In order to derive a fractional extension of the model (13), we introduce the vector

$$D^q_{t_0}\mathbf{c}(t) = \left[D^q_{t_0} c_{dpm}(t), D^q_{t_0} c_{rpm}(t), D^q_{t_0} c_{bio}(t), D^q_{t_0} c_{hum}(t)\right]^{\mathsf{T}},$$

where each entry represents the Caputo time derivative of order $q \in (0,1]$ for the SOC concentration components [40,41].

Ensuring dimensional correctness involves dividing all terms on the right side of (13) by the function $\zeta(t,q)$, characterized by dimensions of T^{q-1} [14]. This dimensional adjustment results in the fractional in-depth RothC model:

$$D^q_{t_0}\mathbf{c}(t) = \frac{\partial}{\partial z}\left(\overline{D}(z,t)\,\frac{\partial \mathbf{c}}{\partial z} - \overline{v}(z,t)\,\mathbf{c}\right) + \overline{\rho}(z,t)\,A\,\mathbf{c} + \overline{\mathbf{b}}_d(z,t), \;\; z \in [0,l], \;\; t \ge t_0. \tag{18}$$

where $\overline{D}(t) = D/\zeta(t,q)$, $\overline{\rho}(z,t) = \rho(z,t)/\zeta(t,q)$ and $\overline{\mathbf{b}}_d(z,t) = \mathbf{b}_d(z,t)/\zeta(t,q)$. Advection velocity is calculated as

$$\overline{v}(z,t) = \overline{K}(z,t)\left(\frac{\partial h(z,t)}{\partial z} - 1\right), \;\; \overline{K}(z,t) = K(z,t)/\zeta(z,t). \tag{19}$$

[1] $k_1(T_{\text{emp}})$, $k_2(s_\theta)$, and $k_3(c)$ correspond respectively to the factors a, b, and c in [32].

For the case $q = 1$, the classical order derivative is recovered.

Examples of ζ functions can be found in [42]. One simple choice, $\zeta(t, q) = 1$, implies that the rates in a medium with memory effects are equivalent to the rates in an ordinary medium. Another option suitable for the fractional-order RothC model is $\Gamma(2-q)t^{q-1}$ where $t \geq t_0 \geq 0$. The usage of the last variant assures $\zeta(z,t)D^q_{t_0} t = 1$.

Regarding the well-posedness of the time-fractional Eq. (18) with the Caputo derivative, we refer to [43], where the existence and uniqueness of its solutions in the case of time and space dependent coefficients have been proven for the case of Dirichlet boundary conditions, considering time and space dependent coefficients. Even though not directly applicable in our context, we wish to cite a very recent result concerning the Richards equation with an integral source term that models root water uptake [44].

4. Greenhouse gas emissions from wetlands

The microbial respiration or organic matter mineralization process in sediments can lead to the release of carbon dioxide (CO_2) and methane (CH_4) into the atmosphere. While the present model accounts for the transfer and decomposition of SOC compounds in the sediment, it does not directly simulate the emission of these gases into the atmosphere. On the other hand, the RothC model can be used in (18) to estimate the amount of carbon that will be emitted.

The spatial distribution of the total carbon retained in the four active pools, denoted as $SOC(z,t)$ [M L^{-3}], is the sum of these individual pool concentrations in the entire column at a given time t, i.e.

$$SOC(z,t) = \mathbf{1}^\top \mathbf{c}(z,t) = c_{\mathrm{dpm}}(z,t) + c_{\mathrm{rpm}}(z,t) + c_{\mathrm{bio}}(z,t) + c_{\mathrm{hum}}(z,t). \tag{20}$$

The rate of change of $SOC(z,t)$ with respect to time can be evaluated as:

$$\begin{aligned} D^q_{t_0} SOC(z,t) &= \sum_{i\in I}\left[\frac{\partial}{\partial z}\left(\overline{D}\,\frac{\partial \mathbf{c}_i}{\partial z} - \overline{v}\,\mathbf{c}_i\right) + \overline{\rho}\,(A\,\mathbf{c})_i + (\overline{\mathbf{b}}_d)_i\right] \\ &= \sum_{i\in I}\left[\frac{\partial}{\partial z}\left(\overline{D}\,\frac{\partial \mathbf{c}_i}{\partial z} - \overline{v}\,\mathbf{c}_i\right) + (\overline{\mathbf{b}}_d)_i\right] + \sum_{i\in I}\overline{\rho}\,(A\,\mathbf{c})_i, \end{aligned}$$

where $I = \{\mathrm{dpm}, \mathrm{rpm}, \mathrm{bio}, \mathrm{hum}\}$.

In the equation above the final sum, which is negative, represents the amount of carbon lost from the system over time due to decomposition. We denote this quantity by $E(z,t)$ [M L^{-3} T^{-q}], defined as

$$E(z,t) := -\sum_{i\in I}\overline{\rho}(z,t)(A\,\mathbf{c})_i = (1-\alpha-\beta)\,\overline{\rho}(z,t)\,\mathbf{k}^\top \mathbf{c}(z,t) > 0. \tag{21}$$

The parameters α and β, along with the components of the vector $\mathbf{k}$, namely k_{dpm}, k_{rpm}, k_{bio}, and k_{hum}, are defined in Eq. (12) and influence the carbon dynamics within the system.

In the following section, we model the emission fluxes of both CO_2 and CH_4 in a wetland. This is achieved using the carbon flux given in (21). We differentiate between unsaturated layers, where only the CO_2 emission flux $E_{CO_2}(z,t)$ is present, and saturated layers, where both $E_{CO_2}(z,t)$ and $E_{CH_4}(z,t)$ fluxes are active. When simulating long-term impact of wetlands on carbon storage and emission, we neglect the processes of gas transport towards the sediment surface and consider instantaneous transfer of gases across the sediment to the water and/or the atmosphere.

To evaluate the CO_2 and CH_4 emissions from the column $[0, l]$ at a given time t, we distinguish between the unsaturated $[0, \overline{z}(t)]$ and saturated $[\overline{z}(t), l]$ layers. When the column is entirely unsaturated, we assume $\overline{z}(t) = l$; when it is entirely saturated, we assume $\overline{z}(t) = 0$; otherwise, $\overline{z}(t)$ corresponds to the water table level between 0 and l.

4.1. Carbon dioxide emissions in the unsaturated sediment layer

In the unsaturated sediment layer $[0, \overline{z}(t)]$, where $h(z,t) < 0$, all the carbon amount $E(z,t)$ is transformed into carbon dioxide due to the aerobic respiration of bacteria. Consequently, the amount of CO_2 respiration from the unsaturated layer at time t is given by

$$ET^u_{CO_2}(t) = \int_0^{\overline{z}(t)} E(z,t)\,dz,$$

and the cumulative value of CO_2 respiration $R^u_{CO_2}(t_0,t_1)$ [M L^{-2}] from the unsaturated sediment layer in the period from $t = t_0$ to $t = t_1$ is

$$R^u_{CO_2}(t_0,t_1) = I^{1-q}_{t_0}\, ET^u_{CO_2}(t_1)$$

where $I^{1-q}_{t_0} f(t) = \dfrac{1}{\Gamma(q)}\int_{t_0}^t f(\tau)(t-\tau)^{q-1}\,d\tau$ is the Riemann–Liouville integral. In the integer-order case ($q = 1$), $R^u_{CO_2}(t_0,t_1) = \int_{t_0}^{t_1} ET^u_{CO_2}(\tau)\,d\tau$.

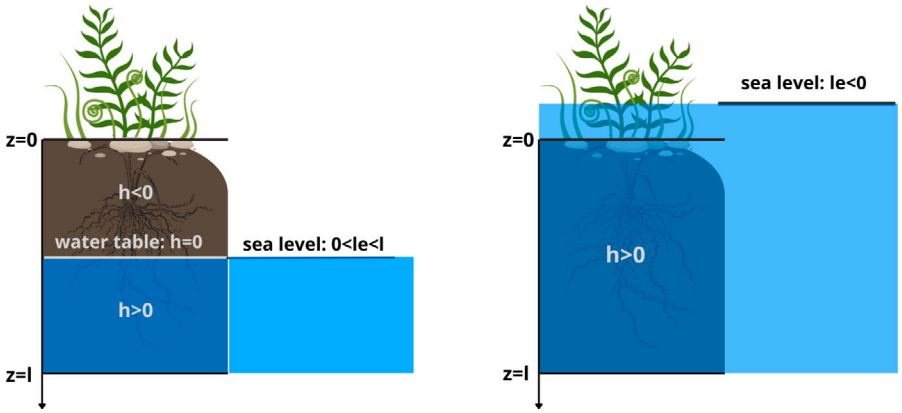

Fig. 1. A graphical representation of a hypothetical column of partially saturated substrate (left) and saturated substrate during flooding (right).

4.2. Carbon dioxide and methane emissions in the saturated sediment layer

In the saturated sediment layer $[\overline{z}(t), l]$, where $h(z,t) \geq 0$ and the sediment can be covered by a water layer, the SOC decomposition is mainly due to the activity of anaerobic bacteria which transform organic carbon into methane (CH_4). However, not all the amount $E(z,t)$ is transformed into methane. Indeed, a portion of the carbon contained in the organic matter can still undergo oxidation even under saturated conditions. In addition, a fraction of the methane produced by anaerobic decomposition in the saturated sediment could be oxidized to carbon dioxide while crossing a thin aerobic layer at the sediment–water interface, before entering the overlying water layer. Both these processes lead to the emission of CO_2 instead of methane.

For simplicity, here we assume that a dimensionless fraction ω of organic matter becomes oxidized, with $0 < \omega < 1$. By defining $ET(t)$ $[\mathrm{M\,L^{-2}\,T^{-q}}]$ as

$$ET(t) = \int_{\overline{z}(t)}^{l} E(z,t)\,dz, \tag{22}$$

the total gas emissions from the saturated sediment layer at time t are thus

$$ET_{CH_4}(t) = (1-\omega)\,ET(t), \qquad ET^{s}_{CO_2}(t) = \omega\,ET(t).$$

Finally, the total amounts of CO_2 and CH_4 emission from a saturated sediment layer in the period from $t = t_0$ to $t = t_1$ are

$$R_{CH_4}(t_0,t_1) = (1-\omega)\,I^{1-q}_{t_0}\,ET(t_1), \quad R^{s}_{CO_2}(t_0,t_1) = \omega\,I^{1-q}_{t_0}\,ET(t_1).$$

In the simulations detailed in the following section, we fixed $\omega = 0.75$. This value is slightly above the estimated ranges, see e.g. [45], and was chosen to ensure that the simulated annual CH_4 emissions from a 1-meter sediment layer are 0.0294 $\mathrm{kg/m^2}$, slightly above the range of 0.0105–0.0262 $\mathrm{kg/m^2}$ reported in [46] for our simulated scenarios, i.e., rice cultivation in delta rivers.

4.3. Global carbon dioxide emissions

The carbon dioxide emission from the entire column at a time t is evaluated as the sum of carbon dioxide produced in both saturated and unsaturated layers, as:

$$ET_{CO_2}(t) = ET^{u}_{CO_2}(t) + ET^{s}_{CO_2}(t)$$

Similarly, the total carbon dioxide emission in a time interval $[t_0, t_1]$ is given by the following sum:

$$R_{CO_2}(t_0,t_1) = R^{u}_{CO_2}(t_0,t_1) + R^{s}_{CO_2}(t_0,t_1).$$

5. Simulations and analysis

Our aim here is to simulate the effects of periodic flooding and sediment moisture fluxes on the balance of sediment carbon stocks and greenhouse gas emissions in a coastal wetland. In addition, we seek to estimate the effectiveness of restoration actions in modifying the carbon storage and fluxes. The reference domain is an idealized substrate column with vertical thickness l which undergoes periodic flooding, as depicted in Fig. 1. We set $z = 0$ at the sediment upper surface. This scenario is inspired by the Ebro Delta region, situated in northeastern Spain near the mouth of the Ebro River, where flooding is routinely practiced for rice cultivation. The area is included among the case studies of RESTORE4Cs, an ongoing Horizon Europe project, which focuses on the role of restoration in improving the greenhouse gas abatement potential of coastal wetlands.

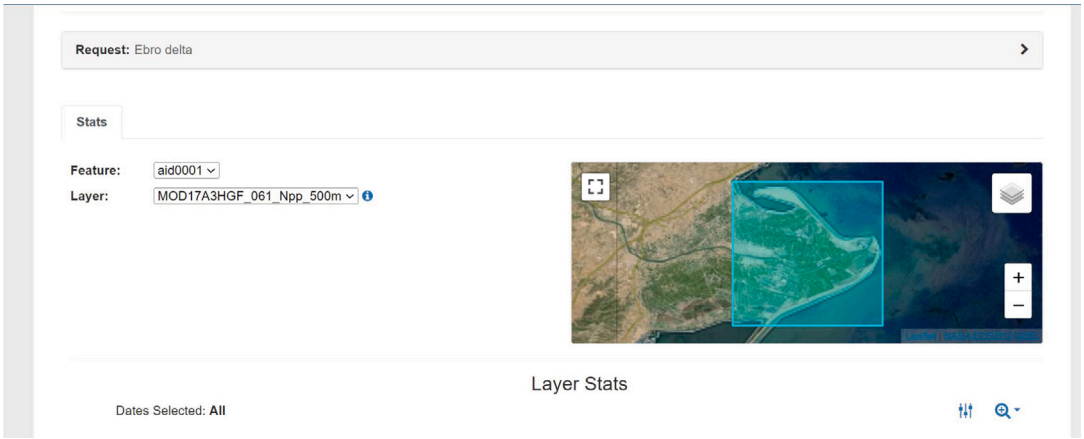

Fig. 2. Selected layer for the Ebro Delta area from the MODIS project of the NASA program (product mod17a3 h).

5.1. Data and parameters

We outline the three differential equations that constitute our model, accompanied by explanations regarding the data and parameters utilized for conducting simulations.

Heat equation for sediment temperature (16). The fixed parameters for heat capacity and thermal conductivity were set as $C_{T_{\text{emp}}} = 2.2 \times 10^6\,\text{J}\,\text{m}^{-3}\,\text{K}^{-1}$ and $\lambda = 3.57\,\text{W}\,\text{m}^{-1}\,\text{K}^{-1}$, corresponding to the values for clay loam [47]. To derive the function $T_a(t)$ for the boundary conditions (17), we used a linear change in averaged air temperature data[2] in the period 1991–2021 from the city of Amposta (Spain), the nearest to the Ebro Delta (see Table 2). Moreover, we set a constant initial distribution of sediment temperature $T_0(z) = 9.3$ °C to match the air temperature $T_a(\text{Jan})$ for January.

Richardson-Richards equation for water head (1). The fixed parameters for RRE, along with their respective references, are summarized in Table 1. According to [8], rice fields are flooded from the end of April to September–October. To model this, we implemented a linear change of the water level $l_e(t)$ from the value of 0.67 m below bottom depth in January ($l_e = 0.67\,\text{m}$, the median surface level above the mean sea level reported in [48]) to the level of 25 cm above sediment surface in June ($l_e = -0.25\,\text{m}$). The function $l_e(t)$ was incorporated into the Dirichlet condition (7) on the bottom side of the domain. For Neumann condition (6) on the upper side, precipitation and evapotranspiration data are required when water does not gather on the sediment surface. Averaged precipitation data in the period 1991–2021 from the city of Amposta are provided in Table 2. Additionally, using temperature data, evapotranspiration was calculated according to the Hargreaves–Samani formula [49], which uses the average annual air temperature $\overline{T}_{\text{emp}}(z)$ set as a constant value of 287.63 K (14.48 °C). The initial distribution of water head $h_0(z)$ was taken as the steady-state solution of RRE, by solving Eq. (11), when $\bar{q} = P(Jan) - ET(Jan) = 6 \cdot 10^{-9}$ m/s and $\bar{l}_e = l_e(Jan) = 0.67$ m.

Fractional RothC model (18). The fixed parameters for the fractional RothC model are provided in Table 3, along with their references. The initial content of SOC compounds was considered equal among them, with their sum obtained from the data provided in [8]. Specifically, using a bulk density of 1770 kg/m^3 and a percentage of SOC content equal to 0.63%, we calculated $C_0 = 0.0063 \times 1770 = 11.12\ \text{kg}/\text{m}^3$. The sediment cover factor values are detailed in Table 2: $k_3(c)$ was set equal to 0.6 from June to September, indicating covered sediment, and 1 during other months, indicating bare sediment. We used Net Primary Productivity (NPP) values as an estimate of total sediment carbon input, as suggested by [11] and further justified by the findings in [50]. These findings include a comparison between litter input derived from solving the inverse problem for the RothC model and NPP values obtained from remote sensing estimates. The annual NPP value was set at 0.5 kg/m^2 per year, falling within the range estimated using remote sensing techniques by MODIS[3] for the territory of Ebro Delta in 2022 [51] (refer to Figs. 2, 3). Furthermore, assuming a constant ratio of NPP to gross primary production (GPP), as suggested in previous studies (see, for example, [52]), we utilized the MODIS GPP product with an 8-day time scale for the year 2023 to calculate the yearly NPP/GPP rate (equal to 0.488). Subsequently, we assessed the distribution of NPP and, consequently SOC input, throughout the year.

The resulting values are summarized in Table 2. Finally, we assumed that 70% of the SOC input enters the model in the form of root-derived products ($\mathbf{B}_d$), while the remaining portion enters through the sediment surface ($\mathbf{b}_s$). The exponent b_e used for the spatial distribution of $\mathbf{b}_d$ in Eq. (14) was set to 5.

[2] https://en.climate-data.org/europe/spain/catalonia/amposta-56879/.

[3] product mod17a3 h. Accessed by: AppEEARS Team. (2024). Application for Extracting and Exploring Analysis Ready Samples (AppEEARS). Ver. 3.48. NASA EOSDIS Land Processes Distributed Active Archive Center (LP DAAC), USGS/Earth Resources Observation and Science (EROS) Center, Sioux Falls, South Dakota, USA. Accessed March 22, 2024. https://appeears.earthdatacloud.nasa.gov.

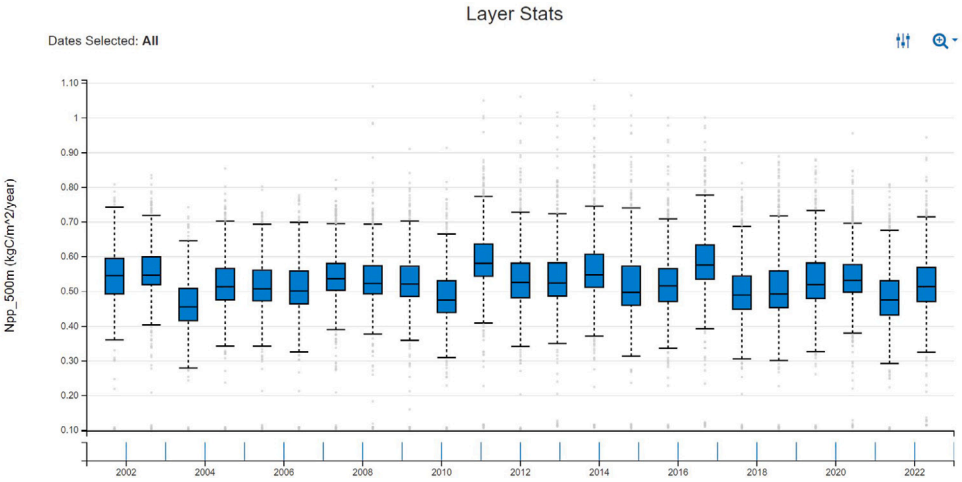

Fig. 3. A box plot of NPP data in the Ebro delta layer spanning the period from 2000 to 2022.

Table 1
Fixed parameter values for RRE (1) obtained using Rosetta v.1 model on the base of midrange values of clay, silt, and sand content for riparian land R1 (subsoil horizon) from [8].

Param.	Description	Value & Dim.
θ_r	Residual water content	0.098
θ_s	Saturated water content	0.422
a	van Genuchten parameter	$0.5\,\mathrm{m}^{-1}$
n	van Genuchten parameter	1.436
K_s	Filtration coefficient	1.37×10^{-7} $\mathrm{m\,s}^{-1}$
η	Mualem parameter	0.678
S_s	Specific storage [53]	range 10^{-5}–10^{-3} m^{-1}

Table 2
Average annual values for temperature (Temp), evapotranspiration (ET), precipitation (P) and level of external water table $l_e(t)$ entering the RRE as boundary conditions. The average annual values of SOC input (NPP - 70% enters the model as $\mathbf{B}_d$, while 30% enters as $\mathbf{b}_s$) and sediment cover factors entering in the fractional-order in-depth RothC model (18) are reported in the last two columns.

Month	Temp (C°)	ET ($\mathrm{m\,s}^{-1}$)	P ($\mathrm{m\,s}^{-1}$)	$\mathbf{l}_e$ (m)	NPP ($\mathrm{kg\,m}^{-2}\,\mathrm{s}^{-1}$)	k_c
Jan	9.3	$1.1\cdot10^{-8}$	$1.7\cdot10^{-8}$	0.5	$3.54\cdot10^{-9}$	1.00
Feb	9.7	$1.4\cdot10^{-8}$	$1.3\cdot10^{-8}$	0.3125	$3.54\cdot10^{-9}$	1.00
Mar	12.1	$2.1\cdot10^{-8}$	$1.6\cdot10^{-8}$	0.125	$5.82\cdot10^{-9}$	1.00
Apr	14.4	$3.0\cdot10^{-8}$	$2.1\cdot10^{-8}$	−0.0625	$7.07\cdot10^{-9}$	1.00
May	17.7	$3.9\cdot10^{-8}$	$2.2\cdot10^{-8}$	−0.25	$7.07\cdot10^{-9}$	1.00
Jun	22	$4.9\cdot10^{-8}$	$1.1\cdot10^{-8}$	−0.25	$2.76\cdot10^{-8}$	0.60
Jul	24.6	$5.1\cdot10^{-8}$	$8.9\cdot10^{-9}$	−0.25	$4.91\cdot10^{-8}$	0.60
Aug	24.8	$4.8\cdot10^{-8}$	$1.4\cdot10^{-8}$	−0.25	$4.38\cdot10^{-8}$	0.60
Sep	21.9	$3.8\cdot10^{-8}$	$2.7\cdot10^{-8}$	−0.25	$2.78\cdot10^{-8}$	0.60
Oct	18.3	$2.7\cdot10^{-8}$	$2.9\cdot10^{-8}$	−0.0625	$9.58\cdot10^{-9}$	1.00
Nov	13	$1.6\cdot10^{-8}$	$2.0\cdot10^{-8}$	0.125	$3.54\cdot10^{-9}$	1.00
Dec	10	$1.1\cdot10^{-8}$	$1.7\cdot10^{-8}$	0.3125	$3.54\cdot10^{-9}$	1.00

5.2. Simulation results

The simulations explored several different issues. Concerning RRE, our objective was to simulate the dynamics of water head movement under the influence of flooding. Subsequently, we aimed to investigate whether alterations in specific storage (S_s) within its variability range might impact the solutions. We then proceeded to analyze the impacts of integrating both diffusive and advective movements into the original RothC model. Furthermore, we examined the potential benefits of introducing fractional order derivatives on the distribution of sediment organic carbon (SOC) compounds within the spatial domain. Lastly, the proposed coupled REE and in-depth RothC model was validated by examining the effects of a flooding program on a restored wetland, specifically in terms of carbon sequestration and greenhouse gas emissions.

Numerical solutions were obtained using a finite-difference approach with central-difference approximation of the first-order spatial derivative and L1-scheme to approximate time-fractional Caputo derivative (see Appendix A). In our simulations we

Table 3
Fixed parameters for the in-depth RothC model.

Param.	Description & Ref	Value & Dim.
D	Diffusivity: Higher value in [54], lower one in [15]	$[10^{-9},\ 10^{-12}]\,\mathrm{m^2\,s^{-1}}$
$clay$	Clay content: Midrange value for riparian land R1 (subsoil horizon) from [8]	24.5%
r	DPM/RPM ratio. Value for improved grassland from [32].	$0.\overline{6}$
k_{dpm}	DPM decomposition rate [32]	$3.21 \cdot 10^{-7}\,\mathrm{s^{-1}}$
k_{rpm}	RPM decomposition rate [32]	$9.64 \cdot 10^{-9}\,\mathrm{s^{-1}}$
k_{bio}	BIO decomposition rate [32]	$2.12 \cdot 10^{-8}\,\mathrm{s^{-1}}$
k_{hum}	HUM decomposition rate [32]	$6.55 \cdot 10^{-10}\,\mathrm{s^{-1}}$
f_{anox}	Rate modifier factor due to anaerobic respiration [13]	0.025

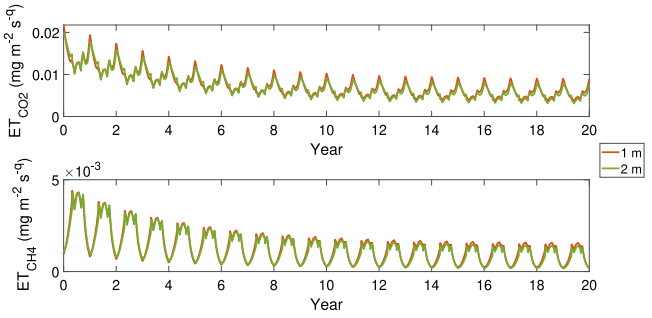

Fig. 4. CO_2 and CH_4 respiration from 1 m layer for different soil column depths.

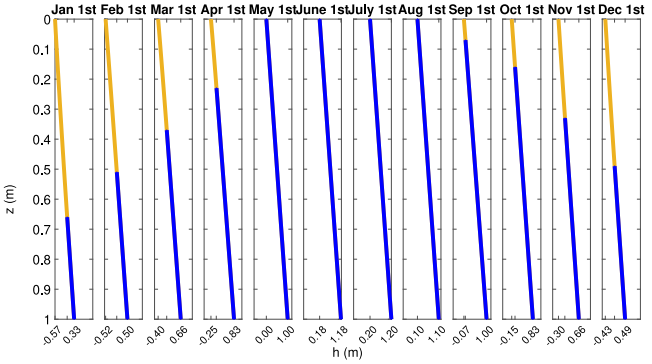

Fig. 5. In-depth water head ($h(z,t)$) profiles over a one year simulation, from RRE (1). red lines indicate positive values (saturated layer) and yellow lines indicate negative values (unsaturated layer). Parameter: $S_s = 10^{-3}\,\mathrm{m^{-1}}$. (For interpretation of the references to color in this figure legend, the reader is referred to the web version of this article.)

considered a uniform spatial grid of 100 points of the substrate column with length of $l = 1$ m, and time-nonuniform finite-difference grid with maximum step length set to one day. For approximating the integral quantities related to the greenhouse gas fluxes we employed the rectangular quadrature rule as detailed in Appendix B.

Influence of flooding on the movement of the water head. We consider how the water table responds to the temporal variation of the boundary condition $l_e(t)$ provided by (7).

Both during flooding, when groundwater moves towards the surface, and during drying, when the sediment becomes directly exposed to the air, it took up to 7 days for the simulated water table level to reach the value imposed by the bottom boundary condition. However, this discrepancy increases with the increase of soil column's depth. Because of the increasing influence of evapotranspiration and precipitation on the upper layer of soil, in which most CO_2 respiration occurs, this in turn leads to the changes in yearly dynamics of CO_2 respiration from 1 m layer passing from 1 m to 2 m depth of the column (Fig. 4). No significant influence of soil column's depth on CH_4 respiration was observed.

Influence of specific storage S_s and diffusivity D on simulation results. In our simulations, the changes of specific storage in the range $[10^{-5}, 10^{-3}]$ did not lead to significant changes in the solutions of RRE over a one-year time period. In Fig. 5, we report the approximated values of water head $h(z,t)$ for the specific storage set at $S_s = 10^{-3}$. In Fig. 6 the corresponding solution of heat equation for sediment temperature $T_{\mathrm{emp}}(z,t)$ is depicted.

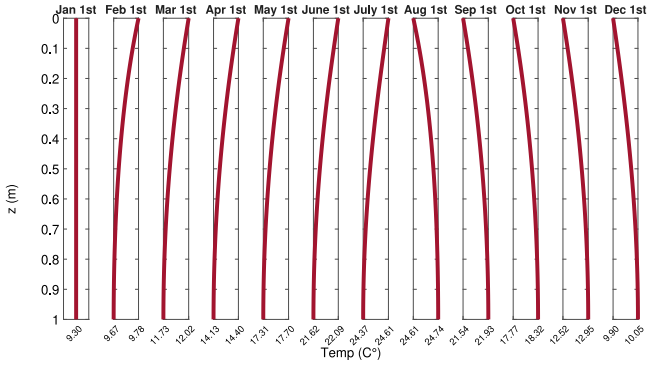

Fig. 6. In-depth temperature profiles from the heat equation (16). Parameter: $S_s = 10^{-3}\ \mathrm{m}^{-1}$.

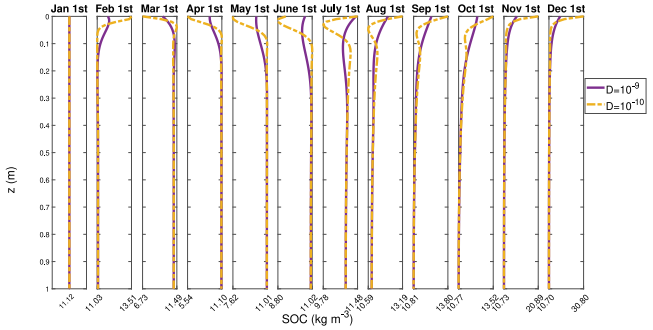

Fig. 7. In-depth SOC profiles over a one year simulation, from the integer-order RothC model (13) with two different diffusivity coefficients. Parameter: $S_s = 10^{-3}\ \mathrm{m}^{-1}$.

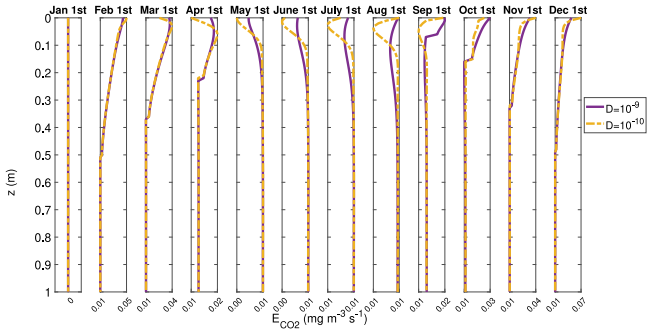

Fig. 8. In-depth CO_2 emission ($E_{CO_2}(z,t)$) profiles over a one year simulation, from in-dept integer-order RothC model (13) with two different diffusivities. Parameter: $S_s = 10^{-3}\ \mathrm{m}^{-1}$.

Throughout the year, we observed minimal changes in the total amount of carbon in the entire column, $\int_0^l SOC(z,t), dz$, when diffusivity was changed from $D = 10^{-9}$ to 10^{-10}. A slightly higher SOC content was obtained for $D = 10^{-9}$. For different values of D the spatial distribution of SOC content gave the higher differences near the surface (see Fig. 7) and interchanging zones of higher and lower respiration are shown in Figs. 8–9.

Influence of velocity field and fractional derivative's order on simulation results. A period of 20 years was simulated using the fractional-order model for three cases: (1) $q = 1$ (integer order); (2) $q = 0.97$, $\zeta(z,t) = 1$; (3) $q = 0.97$, with $\zeta(z,t) = \Gamma(2-q)t^{q-1}$ set as a power function (Figs. 10–11). When $\zeta(z,t)$ had the form of power function, we observed a slight decrease in the greenhouse gas emission compared to the integer-order case (Figs. 10–11).

In the case of $\zeta(z,t) = 1$, respiration had an opposite behavior: compared to the integer-order model, the greenhouse gas emissions were larger.

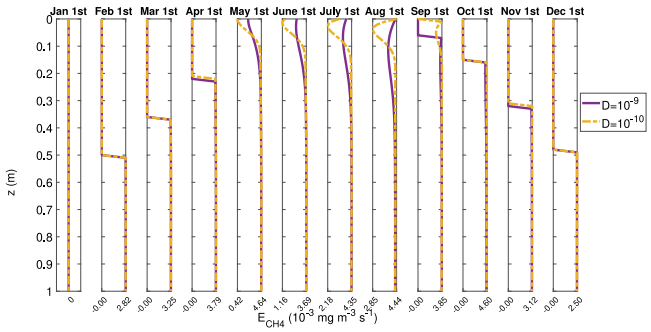

Fig. 9. In-depth CH_4 emission ($E_{CH_4}(z,t)$) profiles over a one year simulation, from in-dept integer-order RothC model (13) with two different diffusivities. Parameter: $S_s = 10^{-3}\ \mathrm{m}^{-1}$.

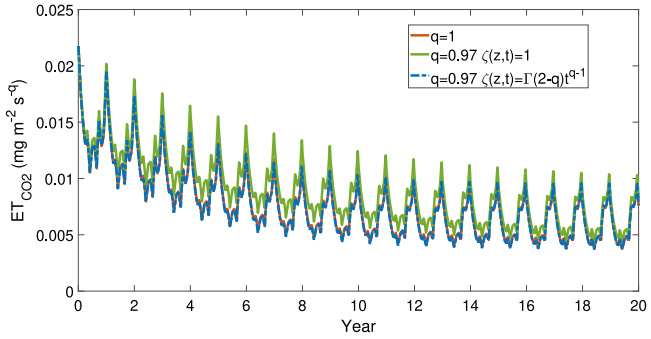

Fig. 10. Dynamics of CO_2 respiration over a 20-year simulation of the in-depth fractional-order RothC model (18). Parameters: $S_s = 10^{-3}\ \mathrm{m}^{-1}$, $D = 10^{-9}\ \mathrm{m}^2\ \mathrm{s}^{-1}$.

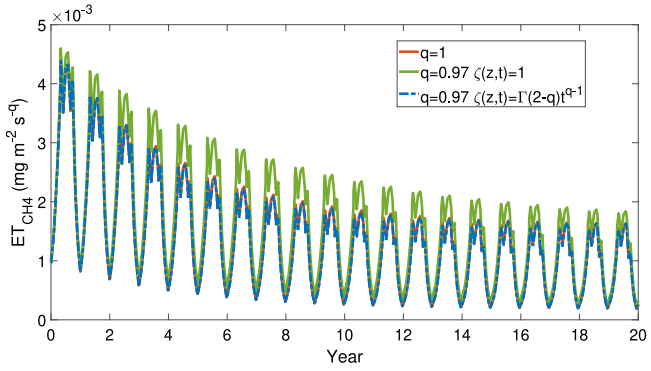

Fig. 11. Dynamics of CH_4 respiration over a 20-year simulation of the in-depth fractional-order RothC model (18). Parameters: $S_s = 10^{-3}\ \mathrm{m}^{-1}$, $D = 10^{-9}\ \mathrm{m}^2\ \mathrm{s}^{-1}$.

When SOC compounds transport is modeled without taking into account advection movements due to the sediment moisture, higher total respiration of both CO_2 and CH_4 is observed during the whole simulated period. In this case lower changes in SOC content are observed near the surface (Fig. 12).

Flooding scenario. As an example, the model was run on the flooding scenario described in [55]. We simulated changes in CH_4 respiration when the coastal wetland used for agricultural production, in this case rice growing, was flooded to revert it to its natural state. We assumed that in the natural state the wetland sediments were constantly covered by 25 cm of water, as described in [55].

First we modeled 20 years in the rice growing scenario, with l_e varying according to the values given in Table 2. Assuming that SOC compounds are in the state close to equilibrium at the initial moment of time, we used the classical RothC model with respiration rate assessed for $t = 0$ to obtain the approximation to such an equilibrium setting the SOC inputs as $M \cdot NPP$ and fitting M to have total SOC amount equal to C_0 [35]. As the result we have $\mathbf{c}_0(z) = [0.38, 5.54, 0.79, 4.47]^T\ \mathrm{kg/m}^3$ with $M = 1/1.75$. A simulation for several years was then performed to obtain in-depth distribution $\mathbf{c}_0(z)$ in a close-to-steady state.

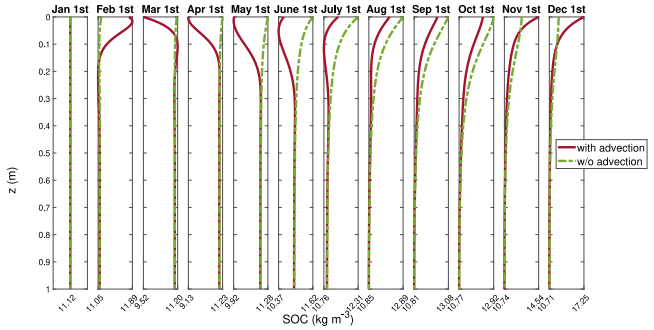

Fig. 12. In-depth SOC profiles over a one year simulation, from in-dept integer-order RothC model (13) with and without advection term. Parameters: $S_s = 10^{-3}$ m^{-1}, $D = 10^{-9}$ m^2 s^{-1}.

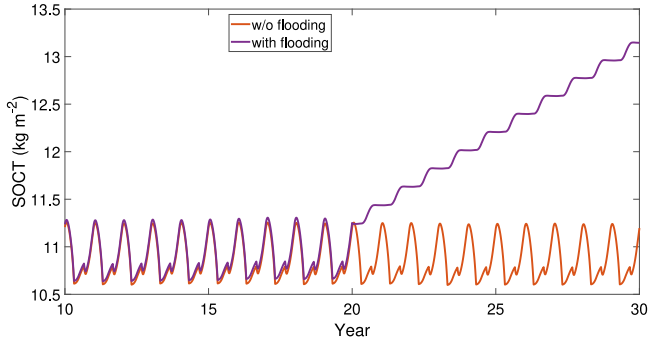

Fig. 13. Temporal dynamics of total SOC, 10 years before and 10 years after flooding. Parameters: $S_s = 10^{-3}$, $D = 10^{-9}$, $q = 1$.

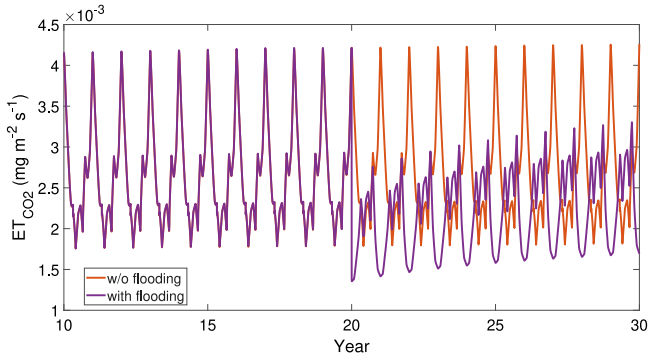

Fig. 14. Temporal dynamics of total CO_2 emission, 10 years before and 10 years after flooding. Parameters: $S_s = 10^{-3}$, $D = 10^{-9}$, $q = 1$.

Afterwards, 20 years were modeled with the constant value $l_e = -0.25$ m. The dynamics of SOC, CO_2 and CH_4 respiration are reported in Figs. 13–15, respectively. The simulated yearly CH_4 respiration for the restored wetland was equal to 0.027 kg/m^2, that is close to the lower bound of the range $0.03 - 0.07$ kg/m^2 reported in Fig. 6e in [55].

6. Discussion and conclusions

In this study, we introduced a novel extension of the RothC model to enhance the modeling of carbon dynamics in wetland sediments. By integrating temporal fractional-order derivatives into spatial dimensions, we developed an adaptive tool capable of capturing the complexities of wetland ecosystems. Our model incorporates Richardson–Richard's equation for moisture fluxes, a diffusion–advection–reaction equation for fractional-order dynamics of SOC compounds, and a temperature transport equation. Through simulations, we investigated the influence of diffusive movement, sediment moisture content, advection terms, and flooding scenarios on carbon dynamics in wetlands.

Compared to the model used in [8], our model takes into account the hydro-physical properties of the saturated and unsaturated sediment, dependencies of decomposition rate on sediment wetness and temperature, and explicitly simulates SOC compounds

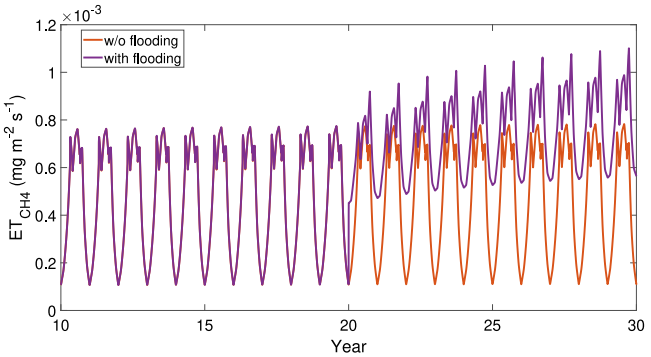

Fig. 15. Temporal dynamics of total CH_4 emission, 10 years before and 10 years after flooding. Parameters: $S_s = 10^{-3}$, $D = 10^{-9}$, $q = 1$.

migration. However, in our model the sediment is considered to have properties which are independent on time, while sediment accretion is simulated in [8].

Compared to the model used in JULES [16], our approach includes an advection term in the equations for the SOC compounds migration. We also consider the time-fractional version of the advection–diffusion–reaction equation. This allows for capturing memory effects on SOC dynamics, which can be caused by processes that are not explicitly modeled (e.g., mass exchange processes between dissolved substances, sediment etc...).

Focusing on coastal wetlands, we implemented a set of boundary conditions based on the assumption that the level of the water table is controlled by external processes such as tidal variations or agricultural flooding/drying. In our approach, the transition processes between the change of water level in the external source and the change of water table depth in the sediment column are assumed to last for a negligible period of time. Such transitional periods were found to be about 7 days, significantly shorter than the monthly computation step used in the RothC model. A similar approach was successfully applied for modeling the influence of ocean surge on groundwater in [56].

Implementing these boundary conditions allowed for the assessment of the impact of advection terms on model solutions, highlighting the importance of considering both hydrological and ecological factors in wetland modeling. Simulations in a 1-meter-deep sediment column showed that water movement can lead to bidirectional migration of SOC compounds to lower sediment horizons.

Furthermore, considering advection terms led to greater variability in the SOC content in the upper 30 cm layer of the sediment.

The introduction of fractional-order derivatives in the model allowed simulating SOC dynamics that, in accordance with previous results (see e.g. [42]), could be either slower or faster than for the classical integer-order case. Thus, fitting the order of the fractional derivative allows one to increase prediction accuracy, adapting the model to the particular conditions in which deviations from the classical behavior occur.

Analyzing the impacts of environmental factors such as diffusive movement and moisture content on the organic carbon dynamics in the sediment, we found that the diffusivity of SOC compounds was an important factor influencing the SOC spatial distribution. As the value of the diffusivity is hard to measure directly, its value, along with the value of the fractional derivative's order, are the model parameters that should be fitted to reproduce the data.

Finally, by assessing wetland flooding scenarios, we illustrated the potential effectiveness of restoration strategies in enhancing carbon sequestration and ecosystem resilience. Our simulations showed lower respiration and SOC outflow from 1 m sediment column following wetland restoration, contributing to understand ecosystem responses to management interventions.

The findings of this study may have significant implications on ecosystem management and conservation efforts. By providing a more comprehensive understanding of sediment carbon dynamics in wetlands, our model can inform decision-making processes related to wetland conservation, restoration, and sustainable land management practices. Furthermore, our approach highlights the importance of considering spatial and temporal dynamics in ecosystem modeling to improve predictions and support effective environmental management strategies.

While our model offers advancements in modeling wetland sediment carbon dynamics, several challenges and opportunities for improvement remain. A potential development of our modeling approach could involve incorporating changes in soil structure over time. In that case, where stratified soils will be considered, variations in parameters such as specific storage, saturated water content, and residual water content will be considered. Modeling layered soils introduces discontinuities in the coefficients of the equations, which require specific numerical techniques for proper treatment. The numerical techniques presented in [57–60] provide a solid foundation for future enhancements of the model to account for non-homogeneous soil conditions.

Future research should focus on refining model parameters, integrating additional environmental variables, and validating model predictions performing an uncertainty analysis to enhance model accuracy and reliability. Further developments could explore additional complexities in wetland ecosystems, such as interactions between carbon and nutrient cycles, vegetation dynamics, and feedback mechanisms. Moreover, efforts to integrate remote sensing data and advanced modeling techniques could enhance the accuracy and applicability of wetland models for real-world management and conservation initiatives.

CRediT authorship contribution statement

Vsevolod Bohaienko: Writing – review & editing, Writing – original draft, Software, Methodology, Investigation, Conceptualization. **Fasma Diele:** Writing – review & editing, Writing – original draft, Supervision, Methodology, Investigation, Conceptualization. **Fabio V. Difonzo:** Methodology, Investigation. **Carmela Marangi:** Writing – review & editing, Supervision, Project administration, Funding acquisition, Conceptualization. **Angela Martiradonna:** Writing – review & editing, Writing – original draft, Software, Methodology, Investigation, Conceptualization. **Antonello Provenzale:** Writing – review & editing, Validation, Supervision, Methodology, Funding acquisition.

Code availability

The C++ codes utilized for the computations showcased in this study, alongside any relevant data, are available for download at https://github.com/CnrIacBaGit/In-Depth-Fractional-RothC.

Acknowledgments

This work has been carried out within the project HORIZON RESTORE4Cs "Modelling RESTORation of wEtlands for Carbon pathways, Climate Change mitigation and adaptation, ecosystem services, and biodiversity, Co-benefits", Grant Agreement No. 101056782 and within the project funded under the National Recovery and Resilience Plan (NRRP), Italy, Mission 4 Component 2 Investment 1.4 - Call for tender No. 3138 of 16 December 2021, rectified by Decree n.3175 of 18 December 2021 of Italian Ministry of University and Research funded by the European Union – NextGenerationEU; Award Number: Project code CN 00000033, Concession Decree No. 1034 of 17 June 2022 adopted by the Italian Ministry of University and Research, CUP B83C22002930006, Project title "National Biodiversity Future Center - NBFC".

Fasma Diele and Fabio V. Difonzo are members of the Gruppo Nazionale Calcolo Scientifico-Istituto Nazionale di Alta Matematica (GNCS-INdAM). Angela Martiradonna is member of GNAMPA-INdAM.

Fabio V. Difonzo acknowledges the support of PRIN2022PNRR n. P2022M7JZW *SAFER MESH - Sustainable mAnagement oF watEr Resources ModEls and numerical MetHods* research grant, funded by the Italian Ministry of Universities and Research (MUR), Italy and by the European Union through Next Generation EU, M4C2, CUP H53D23008930001.

Finally, Fasma Diele and Carmela Marangi would like to thank Mr. Cosimo Grippa for his valuable technical support.

Appendix A. Numerical scheme and computational issues

To obtain numerical solutions we apply a widely used finite-difference approach with central-difference approximation of the first-order spacial derivative and L1-scheme to approximate time-fractional Caputo derivative.

We consider a space-uniform and time-nonuniform finite-difference grid

$$\omega = \left\{ (z_i = ih_z, t_j = t_{j-1} + \tau_j) : \ i = 0, \dots, n; j = 1, 2, \dots \right\}$$

where $h_z = L/n$ is the step with respect to the depth z, τ_j is the length of the step j with respect to the time t. The grid analogue of the function h (and correspondingly the other functions) is defined as $h_{i,j} = h(z_i, t_j)$.

On the grid ω, the derivatives of the function h (and correspondingly the other functions) are approximated the following way [61]:

$$\begin{aligned}
\left.\frac{\partial h(z,t)}{\partial t}\right|_{z=z_i,t=t_{j+1}} &= \frac{h_{i,j+1} - h_{i,j}}{\tau_{j+1}} + O(\tau_{j+1}),\\
\left.\frac{\partial h(z,t)}{\partial z}\right|_{z=z_i,t=t_j} &= \frac{h_{i+1,j} - h_{i-1,j}}{2h_z} + O(h_z^2),\\
\left.\frac{\partial^2 h(z,t)}{\partial z^2}\right|_{z=z_i,t=t_j} &= \frac{h_{i-1,j} - 2h_{i,j} + h_{i+1,j}}{h_z^2} + O(h_z^2),
\end{aligned}$$

The Caputo derivative D_t^q of the concentration functions c_m, $m = 0, \dots, 3$, is approximated as [62]:

$$\begin{aligned}
D_t^q c_m(z,t)\big|_{z=z_i,t=t_j} &= \frac{1}{\Gamma(2-q)} \sum_{k=0}^{j-1} b_{kj}^q \frac{c_{m,i,k+1} - c_{m,i,k}}{\tau_{k+1}} + O\left(\left(\max_j \tau_j \right)^{2-q} \right),\\
b_{kj}^q &= (t_{k+1} - t_j)^{1-q} - (t_k - t_j)^{1-q}.
\end{aligned}$$

Further, we employ the so-called "short memory principle" [63] restricting lower limit of summation to $k = k_j^q : b_{kj}^q < \varepsilon$ where ε is a given accuracy threshold. This imposes additional truncation error, which in the case of fixed time steps τ has, according to [64], an order less than $O(j\tau^{1-q} - \varepsilon^{-1/q}\tau^{\frac{1-q^2}{q}})$.

By employing these approximations and linearizing Eq. (1) representing $K(h,z)$, $C(h,z)$, and $\theta(h,z)$ through the value of h from the previous time step, we derive the following linear system for time step j:

$$h_{i-1,j}\cdot A^{(h)}_{i,j-1}+h_{i+1,j}\cdot B^{(h)}_{i,j-1}+h_{i,j}\cdot R^{(h)}_{i,j-1}=\Phi^{(h)}_{i,j-1},\ i=1,\dots,n-1 \tag{A.1}$$

where:

$$\begin{aligned}
A^{(h)}_{i,j-1}&=\frac{1}{h_z^2}\left(\frac{1}{4}K\left(h_{i+1,j-1}\right)-K\left(h_{i,j-1}\right)-\frac{1}{4}K\left(h_{i-1,j-1}\right)\right),\\
B^{(h)}_{i,j-1}&=\frac{1}{h_z^2}\left(-\frac{1}{4}K\left(h_{i+1,j-1}\right)-K\left(h_{i,j-1}\right)+\frac{1}{4}K\left(h_{i-1,j-1}\right)\right),\\
R^{(h)}_{i,j-1}&=\frac{2K\left(h_{i,j-1}\right)}{h_z^2}+\frac{1}{\tau_{j+1}}\left(C\left(h_{i,j-1}\right)+\frac{\theta(h_{i,j-1},z_k)}{\theta_s}S_s\right),\\
\Phi^{(h)}_{i,j-1}&=\frac{h_{i,j-1}}{\tau_{j+1}}\left(C\left(h_{i,j-1}\right)+\frac{\theta(h_{i,j-1},z_k)}{\theta_s}S_s\right)-\frac{K\left(h_{i+1,j-1}\right)-K\left(h_{i-1,j-1}\right)}{2h_z}.
\end{aligned}$$

The bottom boundary condition takes the form:

$$h_{n,j}=L-L_e(t).$$

For the upper boundary condition, in order to attain a second-order approximation, we utilize the ghost point technique. The resulting equation is obtained by averaging K according to the approach outlined in [65]:

$$h_{0,j}+\frac{A^{(h)}_{0,j-1}+B^{(h)}_{0,j-1}}{R^{(h)}_{0,j-1}}h_{1,j}=\frac{\Phi^{(h)}_{0,j-1}-2\,h_z\,A^{(h)}_{0,j-1}\left(2\frac{E(t_j)-P(t_j)}{K(h_{0,j-1})+K(h_{1,j-1})}+1\right)}{R^{(h)}_{0,j-1}}.$$

Applying the same technique to approximate Eq. (16), we obtain:

$$T_{i-1,j}\cdot A^{(T)}_{i,j-1}+T_{i+1,j}\cdot B^{(T)}_{i,j-1}+T_{i,j}\cdot R^{(T)}_{i,j-1}=\Phi^{(T)}_{i,j-1}\ i=1,\dots,n-1, \tag{A.2}$$

where

$$\begin{aligned}
A^{(T)}_{i,j-1}&=-\frac{\lambda}{h_z^2}-\frac{v_{i,j}}{2h_z}, & B^{(T)}_{i,j-1}&=-\frac{\lambda}{h_z^2}+\frac{v_{i,j}}{2h_z},\\
R^{(T)}_{i,j-1}&=\frac{2\lambda}{h_z^2}+C_{T_{\text{emp}}}w_{i,j}+\frac{C_{T_{\text{emp}}}}{\tau_{j+1}}, & \Phi^{(T)}_{i,j-1}&=\frac{C_{T_{\text{emp}}}T_{i,j-1}}{\tau_{j+1}},\\
T_{0,j}&=T_a(t_j), & T_{n,j}+\frac{A^{(T)}_{n,j-1}+B^{(T)}_{n,j-1}}{R^{(T)}_{n,j-1}}T_{n-1,j}&=\frac{\Phi^{(T)}_{n,j-1}}{R^{(T)}_{n,j-1}}.
\end{aligned}$$

Here,

$$\begin{aligned}
v_{i,j}&=v(z_i,t_j)=K(h_{i,j})\left(\frac{h_{i+1,j}-h_{i-1,j}}{2h_z}-1\right),\\
w_{i,j}&=\frac{\partial v}{\partial z}(z_i,t_j).
\end{aligned}$$

Finally, for Eq. (18), denoting $\overline{v}_{i,j}=v_{i,j}/\zeta(z_i,t_j)$ and $\overline{w}_{i,j}=w_{i,j}/\zeta(z_i,t_j)$, we have for the compartment $m=0,\dots,3$:

$$c_{m,i-1,j}\cdot A^{(c_m)}_{i,j-1}+c_{m,i+1,j}\cdot B^{(c_m)}_{i,j-1}+c_{m,i,j}\cdot R^{(c_m)}_{i,j-1}=-\Phi^{(c_m)}_{i,j-1},\ i=1,\dots,n-1 \tag{A.3}$$

where

$$\begin{aligned}
A^{(c_m)}_{i,j-1}&=-\frac{\overline{D}_m}{h_z^2}-\frac{\overline{v}_{i,j}}{2h_z}, & B^{(c_m)}_{i,j-1}&=-\frac{\overline{D}_m}{h_z^2}+\frac{\overline{v}_{i,j}}{2h_z},\\
R^{(c_m)}_{i,j-1}&=\frac{2\overline{D}_m}{h_z^2}+\overline{w}_{i,j}+\frac{b^q_{j-1,j}}{\Gamma(2-q)\tau_{j+1}},\\
\Phi^{(c_m)}_{i,j-1}&=\frac{b^q_{j-1,j}h_{i,j-1}}{\Gamma(2-q)\tau_{j+1}}-\frac{1}{\Gamma(2-q)}\sum_{k=k^q_j}^{j-2}b^q_{kj}\frac{c_{m,i,k+1}-c_{m,i,k}}{\tau_{k+1}}+\left(\overline{\rho}_{i,j}\,A\,\mathbf{c}_{i,j}+(\overline{\mathbf{b}}_d)_{i,j}\right)_m
\end{aligned}$$

For the boundary conditions we have:

$$c_{m,0,j}+\frac{A^{(c_m)}_{0,j-1}+B^{(c_m)}_{0,j-1}}{R^{(c_m)}_{0,j-1}-2\,h_z\,A^{(c_m)}_{0,j-1}\overline{v}_{0,j-1}/\overline{D}_m}c_{m,1,j}=\frac{\Phi^{(c_m)}_{0,j-1}-2\,h_z\,\frac{A^{(c_m)}_{0,j-1}}{\overline{D}_m}(\mathbf{b}_{\mathbf{s}}(t_j))_m}{R^{(c_m)}_{0,j-1}-2\,h_z\,A^{(c_m)}_{0,j-1}\overline{v}_{0,j-1}/\overline{D}_m},$$

$$c_{m,n,j} + \frac{A^{(c_m)}_{n,j-1} + B^{(c_m)}_{n,j-1}}{R^{(c_m)}_{n,j-1}} c_{m,n-1,j} = \frac{\Phi^{(c_m)}_{n,j-1}}{R^{(c_m)}_{n,j-1}}.$$

To deal with non-linearity, Picard iterations are further applied on the base of the sequential solution of the systems (A.1)–(A.3) finalizing the time-stepping procedure. Linear systems are solved using the TFQMR algorithm [66]. Time steps are dynamically changing according to an empirical procedure on the base of the convergence rate of the TFQMR algorithm.

Appendix B. Numerical evaluation of greenhouse fluxes

Using the rectangular rule quadrature, the CO_2 transpiration $Tr^{(1)}_{CO_2}(t_j)$ at the fractal time moment t_j from the entire sediment column is calculated as

$$Tr^{(1)}_{CO_2}(t_j) = \begin{cases} h_z \sum_{i=0}^{n} \overline{\rho}_{i,j} A \mathbf{c}_{i,j}, & \text{if } h_{i,j} < 0, \\ h_z \omega \sum_{i=0}^{n} \overline{\rho}_{i,j} A \mathbf{c}_{i,j}, & \text{if } h_{i,j} \geq 0. \end{cases}$$

Similarly CH_4 transpiration $Tr^{(1)}_{CH_4}(t_j)$ is calculated as

$$Tr^{(1)}_{CH_4}(t_j) = \begin{cases} 0, & \text{if } h_{i,j} < 0, \\ h_z(1-\omega) \sum_{i=0}^{n} \overline{\rho}_{i,j} A \mathbf{c}_{i,j}, & \text{if } h_{i,j} \geq 0. \end{cases}$$

The total transpirations $Tr^{(2)}_{CO_2}(t_0, t_j)$, $Tr^{(2)}_{CH_4}(t_0, t_j)$ in the period from $t = t_0$ to $t = t_j$ are calculated using L1-approximation of the Riemann–Liouville integral as follows:

$$Tr^{(2)}_{CO_2}(t_0, t_j) = \frac{1}{\Gamma(q+1)} \sum_{k=k_j^{1-q}}^{j-1} b_{kj}^{1-q} \frac{Tr^{(1)}_{CO_2}(t_{k+1}) + Tr^{(1)}_{CO_2}(t_k)}{2},$$

$$Tr^{(2)}_{CH_4}(t_0, t_j) = \frac{1}{\Gamma(q+1)} \sum_{k=k_j^{1-q}}^{j-1} b_{kj}^{1-q} \frac{Tr^{(1)}_{CH_4}(t_{k+1}) + Tr^{(1)}_{CH_4}(t_k)}{2}.$$

References

[1] R.V. Pouyat, D.S. Page-Dumroese, T. Patel-Weynand, L.H. Geiser, Forest and Rangeland Soils of the United States Under Changing Conditions: a Comprehensive Science Synthesis, Springer Nature, 2020.
[2] M.E. Assessment, Ecosystems and Human Well-Being: Wetlands and Water, World Resources Institute, 2005.
[3] D. Russi, P. ten Brink, A. Farmer, T. Badura, C. D, J. Forster, R. Kumar, N. Davidson, The Economics of Ecosystems and Biodiversity for Water and Wetlands, IEEP, London and Brussels; Ramsar Secretariat, Gland, 2021.
[4] Editorial, Valuing wetlands, Nat. Geosci. 14 (2021) 111.
[5] W.R. Moomaw, G. Chmura, G.T. Davies, C. Finlayson, B.A. Middleton, S.M. Natali, J. Perry, N. Roulet, A.E. Sutton-Grier, Wetlands in a changing climate: Science, policy and management, Wetlands 38 (2) (2018) 183–205.
[6] A.W. Mahdiyasa, D.J. Large, B.P. Muljadi, M. Icardi, Modelling the influence of mechanical-ecohydrological feedback on the nonlinear dynamics of peatlands, Ecol. Model. 478 (2023) 110299.
[7] A.W. Mahdiyasa, D.J. Large, M. Icardi, B.P. Muljadi, MPeat2D–a fully coupled mechanical–ecohydrological model of peatland development in two dimensions, Earth Surf. Dyn. 12 (4) (2024) 929–952.
[8] M. Belenguer-Manzanedo, C. Alcaraz, M. Martínez-Eixarch, A. Camacho, J.T. Morris, C. Ibánez, Modeling soil accretion and carbon accumulation in deltaic rice fields, Ecol. Model. 484 (2023) 110455.
[9] Y. Fan, G. Miguez-Macho, A simple hydrologic framework for simulating wetlands in climate and earth system models, Clim. Dyn. 37 (2011) 253–278.
[10] A. Sharifi, M. Hantush, L. Kalin, Modeling nitrogen and carbon dynamics in wetland soils and water using mechanistic wetland model, J. Hydrol. Eng. 22 (1) (2017) D4016002.
[11] Y. Zhang, C. Li, C.C. Trettin, H. Li, G. Sun, An integrated model of soil, hydrology, and vegetation for carbon dynamics in wetland ecosystems, Glob. Biogeochem. Cycles 16 (4) (2002) 9-1–9-17.
[12] J. Smith, P. Gottschalk, J. Bellarby, M. Richards, D. Nayak, K. Coleman, J. Hillier, H. Flynn, M. Wattenbach, M. Aitkenhead, et al., Model to estimate carbon in organic soils–sequestration and emissions (ECOSSE), Carbon 44 (2010) 1–73.
[13] S. Frolking, N. Roulet, T. Moore, P. Lafleur, J. Bubier, P. Crill, Modeling seasonal to annual carbon balance of Mer Bleue Bog, Ontario, Canada, Glob. Biogeochem. Cycles 16 (3) (2002) 1030.
[14] V. Bohaienko, F. Diele, C. Marangi, C. Tamborrino, S. Aleksandrowicz, E. Woźniak, A novel fractional-order RothC model, Mathematics 11 (7) (2023) 1677.
[15] C.D. Koven, W.J. Riley, Z.M. Subin, J.Y. Tang, M.S. Torn, W.D. Collins, G.B. Bonan, D.M. Lawrence, S.C. Swenson, The effect of vertically resolved soil biogeochemistry and alternate soil C and N models on C dynamics of CLM4, Biogeosciences 10 (2013) 7109–7131.
[16] E.J. Burke, S.E. Chadburn, A. Ekici, A vertical representation of soil carbon in the JULES land surface scheme (vn4. 3_permafrost) with a focus on permafrost regions, Geosci. Model. Dev. 10 (2) (2017) 959–975.
[17] D.B. Clark, L.M. Mercado, S. Sitch, C.D. Jones, N. Gedney, M.J. Best, M. Pryor, G.G. Rooney, R.L.H. Essery, E. Blyth, O. Boucher, R.J. Harding, C. Huntingford, P.M. Cox, The joint UK land environment simulator (JULES), model description – part 2: Carbon fluxes and vegetation dynamics, Geosci. Model. Dev. 4 (3) (2011) 701–722.

[18] C. Minaudo, D. von Schiller, M. B., D. Morant, M. Adamescu, K. Attermeyer, A. Basset, R. Carballeira, C. Cazacu, J. Coelho, A. Guelmami, S. Hilaire, J. Miralles, B. Obrador, J. Petkuviene, A. Picazo, C. Rochera, C. Santinelli, H. Teixeira, J. Titocci, D. Vaicute, A. Camacho, Methodological manual. Deliverable D4.2, 2023, Horizon RESTORE4Cs Project GA ID: 101056782.
[19] Y. Zha, J. Yang, J. Zeng, C.-H.M. Tso, W. Zeng, L. Shi, Review of numerical solution of Richardson–richards equation for variably saturated flow in soils, Wiley Interdiscip. Rev.: Water 6 (5) (2019) e1364.
[20] M. Berardi, M. D'Abbicco, G. Girardi, M. Vurro, Optimizing water consumption in Richards' equation framework with step-wise root water uptake: A simplified model, Transp. Porous Media (2022) 1–30.
[21] M. Bause, P. Knabner, Computation of variably saturated subsurface flow by adaptive mixed hybrid finite element methods, Adv. Water Resour. 27 (6) (2004) 565–581.
[22] I.S. Pop, F. Radu, P. Knabner, Mixed finite elements for the Richards' equation: Linearization procedure, J. Comput. Appl. Math. 168 (1–2) (2004) 365–373.
[23] A. Dogan, L. Motz, Saturated-unsaturated 3D groundwater model. I: Development, J. Hydrol. Eng. 10 (6) (2005) 492–504.
[24] J.-B. Clément, D. Sous, F. Bouchette, F. Golay, M. Ersoy, A Richards' equation-based model for wave-resolving simulation of variably-saturated beach groundwater flow dynamics, J. Hydrol. 619 (2023) 129344.
[25] M. van Genuchten, A closed-form equation for predicting the hydraulic conductivity of unsaturated soils, Soil Sci. Soc. Am. J. 44 (1980) 884–900.
[26] Y. Mualem, A new model for predicting the hydraulic conductivity of unsaturated porous media, Water Resour. Res. 12 (3) (1976) 513–522.
[27] C. Hinz, Analysis of unsaturated/saturated water flow near a fluctuating water table, J. Contam. Hydrol. 33 (1–2) (1998) 59–80.
[28] B. Schweizer, The Richards equation with hysteresis and degenerate capillary pressure, J. Differential Equations 252 (10) (2012) 5594–5612.
[29] G. Marinoschi, Functional Approach to Nonlinear Models of Water Flow in Soils, vol. 21, Springer, 2006.
[30] A. Martínez, R. Muñoz-Sola, M. Vázquez-Méndez, L. Alvarez-Vázquez, A local regularity result for Neumann parabolic problems with nonsmooth data, Indag. Math. 28 (2) (2017) 494–515.
[31] G.M. Lieberman, Mixed boundary value problems for elliptic and parabolic differential equations of second order, J. Math. Anal. Appl. 113 (2) (1986) 422–440.
[32] K. Coleman, D. Jenkinson, Rothc-26.3-a model for the turnover of carbon in soil, in: Evaluation of Soil Organic Matter Models: Using Existing Long-Term Datasets, Springer, 1996, pp. 237–246.
[33] A. Parshotam, The rothamsted soil-carbon turnover model—discrete to continuous form, Ecol. Model. 86 (2–3) (1996) 283–289.
[34] F. Diele, C. Marangi, A. Martiradonna, Non-standard discrete RothC models for soil carbon dynamics, Axioms 10 (2) (2021) 56.
[35] F. Diele, I. Luiso, C. Marangi, A. Martiradonna, E. Woźniak, Evaluating the impact of increasing temperatures on changes in soil organic carbon stocks: Sensitivity analysis and non-standard discrete approximation, Comput. Geosci. 26 (5) (2022) 1345–1366.
[36] F. Diele, I. Luiso, C. Marangi, A. Martiradonna, SOC-reactivity analysis for a newly defined class of two-dimensional soil organic carbon dynamics, Appl. Math. Model. 118 (2023) 1–21.
[37] T.G. Morais, R.F. Teixeira, T. Domingos, Detailed global modelling of soil organic carbon in cropland, grassland and forest soils, PLoS One 14 (9) (2019) e0222604.
[38] C. Koven, P. Friedlingstein, P. Ciais, D. Khvorostyanov, G. Krinner, C. Tarnocai, On the formation of high-latitude soil carbon stocks: Effects of cryoturbation and insulation by organic matter in a land surface model, Geophys. Res. Lett. 36 (21) (2009).
[39] A. Elzein, J. Balesdent, Mechanistic simulation of vertical distribution of carbon concentrations and residence times in soils, Soil Sci. Am. J. 59 (5) (1995) 1328–1335.
[40] S. Samko, A. Kilbas, O. Marichev, Fractional Integrals and Derivatives, Gordon and Breach Science Publishers, New York, NY, 1993.
[41] K. Diethelm, N.J. Ford, Analysis of fractional differential equations, J. Math. Anal. Appl. 265 (2) (2002) 229–248.
[42] J. Gomez-Aguilar, M. Miranda-Hernandez, M. Lopez-Lopez, V. Alvarado-Martinez, D. Baleanu, Modeling and simulation of the fractional space-time diffusion equation, Commun. Nonlinear Sci. Numer. Simul. 30 (2016) 115–127.
[43] A. Kubica, M. Yamamoto, Initial-boundary value problems for fractional diffusion equations with time-dependent coefficients, Fract. Calc. Appl. Anal. 21 (2018) 1314–2224.
[44] M. Berardi, G. Girardi, Modeling plant water deficit by a non-local root water uptake term in the unsaturated flow equation, Commun. Nonlinear Sci. Numer. Simul. 128 (2024) 107583.
[45] P. Roslev, G.M. King, Regulation of methane oxidation in a freshwater wetland by water table changes and anoxia, FEMS Microbiol. Ecol. 19 (2) (1996) 105–115.
[46] C. Fertitta-Roberts, P.Y. Oikawa, G.D. Jenerette, Evaluating the GHG mitigation-potential of alternate wetting and drying in rice through life cycle assessment, Sci. Total Environ. 653 (2019) 1343–1353.
[47] T.E. Ochsner, R. Horton, T. Ren, A new perspective on soil thermal properties, Soil Sci. Am. J. 65 (6) (2001) 1641–1647.
[48] A. Genua-Olmedo, C. Alcaraz, N. Caiola, C. Ibáñez, Sea level rise impacts on rice production: The Ebro Delta as an example, Sci. Total Environ. 571 (2016) 1200–1210.
[49] G.H. Hargreaves, Z.A. Samani, Reference crop evapotranspiration from temperature, Appl. Eng. Agric. 1 (2) (1985) 96–99.
[50] M.W. Shoji Hashimoto, P. Smith, Litter carbon inputs to the mineral soil of Japanese brown forest soils: comparing estimates from the RothC model with estimates from MODIS, J. For. Res. 16 (1) (2011) 16–25.
[51] S. Running, M. Zhao, MODIS/Terra net primary production gap-filled yearly L4 global 500 m SIN grid V061, NASA EOSDIS Land Process. DAAC (2021).
[52] B.J. Choudhury, Carbon use efficiency, and net primary productivity of terrestrial vegetation, Adv. Space Res. (ISSN: 0273-1177) 26 (7) (2000) 1105–1108, Remote Sensing for Land Surface Characterisation.
[53] F. Chowdhury, J. Gong, G.C. Rau, W.A. Timms, Multifactor analysis of specific storage estimates and implications for transient groundwater modelling, Hydrogeol. J. 30 (7) (2022) 2183–2204.
[54] K. Yoo, R. Amundson, A.M. Heimsath, W.E. Dietrich, Erosion of upland hillslope soil organic carbon: Coupling field measurements with a sediment transport model, Glob. Biogeochem. Cycles 19 (2005) GB3003.
[55] P.Y. Oikawa, G.D. Jenerette, S.H. Knox, C. Sturtevant, J. Verfaillie, I. Dronova, C.M. Poindexter, E. Eichelmann, D.D. Baldocchi, Evaluation of a hierarchy of models reveals importance of substrate limitation for predicting carbon dioxide and methane exchange in restored wetlands, J. Geophys. Res. Biogeosci. 122 (2017) 145–167.
[56] X. Yu, J. Yang, T. Graf, M. Koneshloo, M.A. O'Neal, H.A. Michael, Impact of topography on groundwater salinization due to ocean surge inundation, Water Resour. Res. 52 (8) (2016) 5794–5812.
[57] M. Berardi, F. Difonzo, M. Vurro, L. Lopez, The 1D Richards' equation in two layered soils: A Filippov approach to treat discontinuities, Adv. Water Resour. 115 (2018) 264–272.
[58] D. Seus, K. Mitra, I.S. Pop, F.A. Radu, C. Rohde, A linear domain decomposition method for partially saturated flow in porous media, Comput. Methods Appl. Mech. Engrg. 333 (2018) 331–355.
[59] K. Kumar, F. List, I.S. Pop, F.A. Radu, Formal upscaling and numerical validation of unsaturated flow models in fractured porous media, J. Comput. Phys. 407 (2020) 109138.
[60] M. Berardi, F. Difonzo, L. Lopez, A mixed MoL–TMoL for the numerical solution of the 2D Richards' equation in layered soils, Comput. Math. Appl. 79 (7) (2020) 1990–2001.

[61] A. Samarskii, P. Vabishchevich, Computational Heat Transfer, Wiley, New York, 1995.
[62] T. Atanackovic, B. Stankovic, On a numerical scheme for solving differential equations of fractional order, Mech. Res. Commun. 35 (7) (2008) 429–438.
[63] N. Ford, A. Simpson, The numerical solution of fractional differential equations: Speed versus accuracy, Numer. Algorithms 26 (2001) 333–346.
[64] V. Bohaienko, Accuracy and speed of splitting methods for three-dimensional space–time fractional diffusion equation with ψ-Caputo derivatives, Math. Comput. Simulation 188 (2021) 226–240.
[65] J. van Dam, R. Feddes, Numerical simulation of infiltration, evaporation and shallow groundwater levels with the Richards equation, J. Hydrol. 233 (2000) 72–85.
[66] R.W. Freund, A transpose-free quasi-minimal residual algorithm for non-Hermitian linear systems, SIAM J. Sci. Comput. 14 (2) (1993) 470–482.